# From Binary $Cu_2S$ to Ternary Cu–In–S and Quaternary Cu–In–Zn–S Nanocrystals with Tunable Composition *via* Partial Cation Exchange

**Quinten A. Akkerman,[†,‡] Alessandro Genovese,[†] Chandramohan George,[†,§] Mirko Prato,[†] Iwan Moreels,[†] Alberto Casu,[†] Sergio Marras,[†] Alberto Curcio,[†] Alice Scarpellini,[†] Teresa Pellegrino,[†] Liberato Manna,[†] and Vladimir Lesnyak[*,†]**

[†]Department of Nanochemistry, Istituto Italiano di Tecnologia, via Morego, 30, 16163 Genova, Italy, [‡]Condensed Matter and Interfaces, Debye Institute for Nanomaterials Science, Utrecht University, 3508 TA Utrecht, The Netherlands, and [§]Institute for Manufacturing, Department of Engineering, University of Cambridge, 17 Charles Babbage Road, Cambridge CB3 0FS, United Kingdom

**ABSTRACT** We present an approach for the synthesis of ternary copper indium sulfide (CIS) and quaternary copper indium zinc sulfide (CIZS) nanocrystals (NCs) by means of partial cation exchange with $In^{3+}$ and $Zn^{2+}$. The approach consists of a sequential three-step synthesis: first, binary $Cu_2S$ NCs were synthesized, followed by the homogeneous incorporation of $In^{3+}$ by an *in situ* partial cation-exchange reaction, leading to CIS NCs. In the last step, a second partial exchange was performed where $Zn^{2+}$ partially replaced the $Cu^+$ and $In^{3+}$ cations at the surface, creating a ZnS-rich shell with the preservation of the size and shape. By careful tuning reaction parameters (growth and exchange times as well as the initial $Cu^+$:$In^{3+}$:$Zn^{2+}$ ratios), control over both the size and composition was achieved. This led to a broad tuning of photoluminescence of the final CIZS NCs, ranging from 880 to 1030 nm without altering the NCs size. Cytotoxicity tests confirmed the biocompatibility of the synthesized CIZS NCs, which opens up opportunities for their application as near-infrared fluorescent markers in the biomedical field.

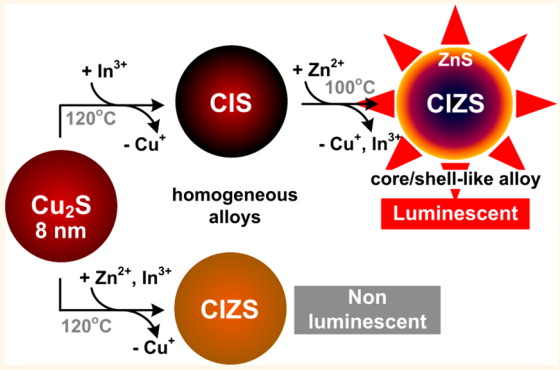


**KEYWORDS:** nanocrystals · copper sulfide · copper indium sulfide · copper indium zinc sulfide · alloys · cation exchange · photoluminescence · Stokes shift engineering · cyclic voltammetry

Colloidal semiconductor nanocrystals (NCs) have attracted great scientific interest due to their extraordinary size-dependent optical and electronic properties. The most promising and studied NCs are the binary II–VI and IV–VI compounds MX (where $M^{2+}$ = Cd, Hg, Pb, and $X^{2-}$ = S, Se, Te), which have been successfully exploited in electronic, optoelectronic, photovoltaic applications, and biolabeling.[1−6] Although state-of-the art synthetic techniques provide stable NCs in a wide variety of sizes and shapes and therefore with tunable optical and electronic properties, they contain toxic elements such as Cd, Hg, and Pb which are a risk when released into the environment. This hinders their widespread applicability, especially in the field of biomedicine, where semiconductor NCs have demonstrated great potential in various techniques, such as bioimaging, sensing, and cell-tracking. In addition, various technological applications of these materials, such as lighting, solar energy conversion, and telecommunications, may be challenging due to their toxicity.

In the past decade, the focus has shifted toward toxic element-free and more abundant binary ($Cu_{2-x}S$, $Cu_{2-x}Se$),[7−10] ternary (Cu:ZnS, $CuInS_2$, $CuInSe_2$, $AgInS_2$),[11−14] and even quaternary (CuInZnS, CuSnZnS, CuInGaS)[13,15,16] semiconductor NCs. Among these copper chalcogenide-based materials, $CuInS_2$ (CIS) has been the most studied semiconductor for both light-absorbing and -emitting applications.[11,13,17−19] CIS has a direct bulk band gap of 1.45 eV and has an exciton Bohr radius of 4.1 nm,[11] making it an

* Address correspondence to vladimir.lesnyak@iit.it.

Received for review October 10, 2014 and accepted December 31, 2014.

**Published online December 31, 2014**
**10.1021/nn505786d**

ideal light absorber for solar cells as well as visible-near-infrared (NIR) light emitter. Although CIS NCs can be luminescent, their photoluminescence (PL) efficiency is often relatively low (<10%), but it can be strongly enhanced by either the incorporation of $Zn^{2+}$ or by growing a ZnS shell.[16,20−23] The PL of these CIZS and CIS/ZnS core/shell NCs can be fine-tuned by controlling the size of the NCs and the Cu:In:Zn ratio.[16,20,24,25]

Colloidal CIS NCs are commonly prepared by a direct synthesis, where all three precursors (*i.e.*, compounds serving as Cu, In, and S sources) are utilized together in one pot, either by using a hot-injection method or heat-up synthesis. If necessary, incorporation of $Zn^{2+}$ ions or ZnS shell coating can be realized in a second step of the synthesis. All aspects of the synthesis of these systems have recently been summarized in excellent comprehensive reviews by Kolny-Olesiak and Weller[11] and Aldakov *et al.*[13] The main drawback of the CIS and CIZS NCs (and ternary and quaternary NCs in general) is the limited size, shape, and composition control due to the complex equilibria in multiple reactions between cation and anion precursors that exhibit different reactivities. Although much effort has been made in the size and shape control of CIS and CIZS, currently only dots, rods, and thick platelets have been reported, and no synthetic approach has been developed yet with full size, shape, and composition control.[26,27] Furthermore, the PL properties have mostly been studied for small (≤4 nm) NCs, whose emission covers the visible region, only in some cases extending to the NIR spectral part. The light-emission of larger particles has not been fully investigated, but it could be potentially interesting for NIR emitters, which can be used in biolabeling and telecommunications.

Taking into account the above-mentioned restrictions of direct multicomponent colloidal synthesis, an appropriate method for achieving size, shape, and composition control would be a preparation of binary chalcogenide nanoparticles with subsequent incorporation of the desired cations into the crystal structure *via* cation-exchange (CE) reactions. In this way, host cations of a parent semiconductor NC can be replaced by guest cations preserving its anionic framework and thus without major altering of the size and shape of the particle (although a slight rearrangement of the anionic sublattice can occur, especially at high temperatures). The main focus of the CE has been on the complete replacement of monovalent and divalent cations including $Ag^{+}$, $Cu^{+}$, $Cd^{2+}$, $Zn^{2+}$, and $Pb^{2+}$, yielding, *e.g.*, complex sized and shaped NCs like PbSe/PbS core/shell NCs and metastable wurtzite ZnS NCs, which are not attainable in a direct synthesis.[28−37] At the same time, partial CE can be used to synthesize ternary or quaternary NCs starting from the corresponding binary (or ternary) compounds with high control over the final composition. For instance, CIZS NCs have recently been synthesized by partial CE with $Zn^{2+}$ starting from CIS particles.[16,38,39] Although the reactions involving monovalent and divalent cations have been extensively investigated, the exchange with trivalent cations like $Ga^{3+}$ and $In^{3+}$ has been reported only by Beberwyck *et al.*, where InAs, InP, GaAs and GaP nanoparticles were synthesized starting from $Cd_3As_2$ and $Cd_3P_2$.[40]

In this work, we present an approach to synthesize ternary CIS and quaternary CIZS NCs *via* a sequential partial CE with $In^{3+}$ and $Zn^{2+}$ ions, starting from $Cu_2S$ NCs. This synthesis method offers full control over the size, shape, and composition of the materials yielding ∼7−8 nm spherical homogeneous alloyed CIS and both homogeneous and core/shell-like alloyed CIZS NCs with tunable PL in the range from 880 to 1030 nm. This approach represents a new route for precisely tailored ternary and quaternary NCs containing trivalent cations. First, monodisperse spherical stoichiometric $Cu_2S$ NCs were synthesized by a novel heat-up method using thiourea as a sulfur source. In the second step, *i.e.* CE reaction, $In^{3+}$ partially replaced $Cu^{+}$ cations. The composition of the obtained CIS NCs can be tuned by varying both the initial In:Cu ratio and the exchange time. The size of the CIS is controlled by the growth time of the parent $Cu_2S$ NCs and ranges from ∼3 to 8 nm. Finally, $Zn^{2+}$ ions were incorporated, replacing both $In^{3+}$ and $Cu^{+}$, leading to the quaternary graded alloy CIZS NCs. As in the case of $Cu^{+} \rightarrow In^{3+}$ exchange, the amount of $Zn^{2+}$ can be controlled by varying the amount of $Zn^{2+}$ precursor and the exchange time. Zinc incorporation leads to a PL maximum blue-shift of over 150 nm without major altering of the size, crystal structure, and absorption properties of the predecessor CIS NCs.

## RESULTS AND DISCUSSION

In order to study the structural properties of CIS and CIZS NCs (in particular, the distribution of elements within the exchanged particles) relatively large (∼8 nm) $Cu_2S$ NCs were synthesized and used as parent particles. Note that after the CE to CIS, the NCs were still within the quantum confinement regime (Bohr diameter of 8.2 nm for CIS). The overall synthetic scheme is shown in Figure 1.

**Synthesis of $Cu_2S$ NCs.** In the first step of the synthesis, $Cu_2S$ NCs were prepared by a novel non-injection method using thiourea as a sulfur source. As Figure 2a indicates, this synthesis yields fairly monodisperse, spherical 7.9 ± 1.0 nm copper sulfide nanoparticles. Their spontaneous self-assembly, shown in Figure SI1 (see the Supporting Information), further confirms the narrow size distribution.[35] The size of these NCs could be controlled by varying the growth time from 0 to 30 min, yielding a series of spherical particles ranging from ∼4.0 to 7.9 nm (see Figure SI2, Supporting Information),

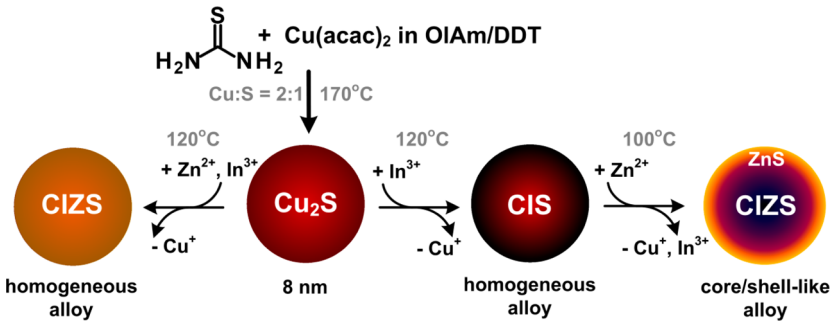


**Figure 1. Scheme of the synthesis of pristine $Cu_2S$ NCs and their exchange reactions to CIS and CIZS NCs possessing both homogeneous (left) and core/shell (right) alloy structures. OlAm = oleylamine, DDT = 1-dodecanethiol.**

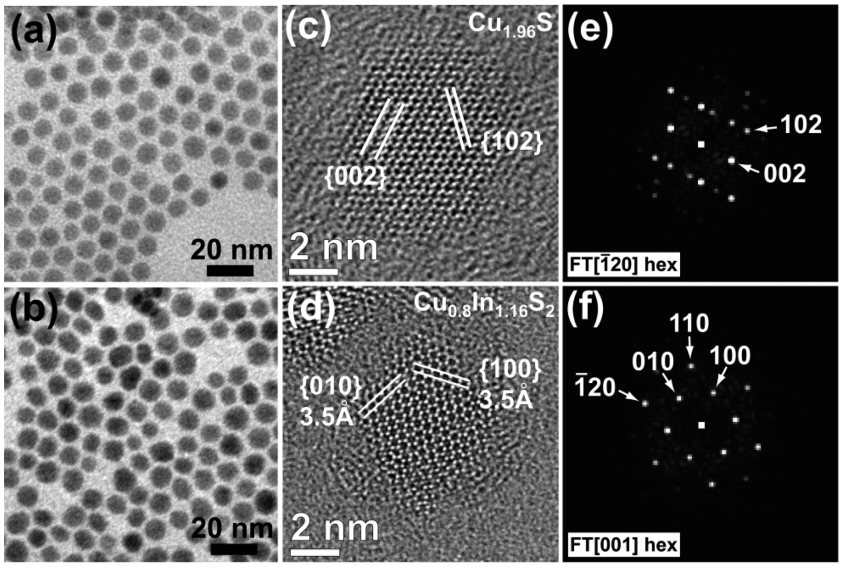


**Figure 2. Conventional transmission electron microscopy (TEM) images of parent $Cu_2S$ NCs (a) and exchanged CIS NCs (b). (c, d) HRTEM characterization of the corresponding NCs displaying their main lattice sets. Fourier transform (FT) analysis of $Cu_2S$ (e) and CIS (f) NCs, consistent with the axial projection [$\bar{1}$20] and [001], respectively, and revealing hexagonal symmetry.**

whereas their shape can be altered from spherical dots to disks by increasing the growth temperature from 170 to 200 °C (see Figure SI3, Supporting Information).

The crystal structure of copper sulfide NCs was investigated by means of high resolution transmission electron microscopy (HRTEM). As revealed by HRTEM data analysis, the particles have a hexagonal crystal structure exhibiting main {002} and {102} lattice sets with *d*-spacing of 3.4 and 2.4 Å, respectively (see Figure 2c). These lattice parameters are compatible with a high chalcocite phase, as shown by the Fourier transform (FT) analysis in Figure 2e, where the reciprocal vector relationship of the crystal structure is consistent with the [$\bar{1}$20] zone axis projection of high chalcocite (ICSD card 43323). High angle annular dark field scanning TEM (HAADF-STEM) images of $Cu_2S$ NCs, as well as CIS and CIZS particles, are shown in Figure SI4 (see the Supporting Information). STEM- energy dispersive X-ray spectroscopy (EDS) analysis yielded an atom quantification of Cu:S = 0.66:0.34, confirming the chemical composition of $Cu_{1.96}S$ chalcocite. Conversely, the powder X-ray diffraction (XRD) pattern of the as-synthesized $Cu_2S$ NCs can be indexed as low chalcocite phase characterized by a monoclinic structure (see Figure 3). As our group has already observed, low symmetry $Cu_2S$ NCs change into high chalcocite structure when exposed to high temperature or to an electron beam.[41] Thus, prepared $Cu_2S$ NCs in the form of a crude reaction mixture were further used for the synthesis of CIS NCs as discussed in the following section.

**Synthesis of CIS NCs: $In^{3+}$ Incorporation.** In order to obtain CIS NCs, we developed a new CE method for the incorporation of $In^{3+}$. In this approach, indium(III) acetylacetonate ($In(acac)_3$) and tri-*n*-octylphosphine (TOP) were introduced at 120 °C into a crude as-prepared $Cu_2S$ NC solution. A relatively low temperature was used to gain control over the amount of incorporated $In^{3+}$ ions. This method is similar to a recently published method for the incorporation of $Zn^{2+}$ and $Sn^{4+}$ into $Cu_{2-x}Se_ySy_{1-y}$ nanodisks[42] and $Sn^{2+}$ ($Sn^{4+}$) into $Cu_{2-x}Se$ spherical particles.[43] Figure 2b shows the NCs after the partial cation exchange,

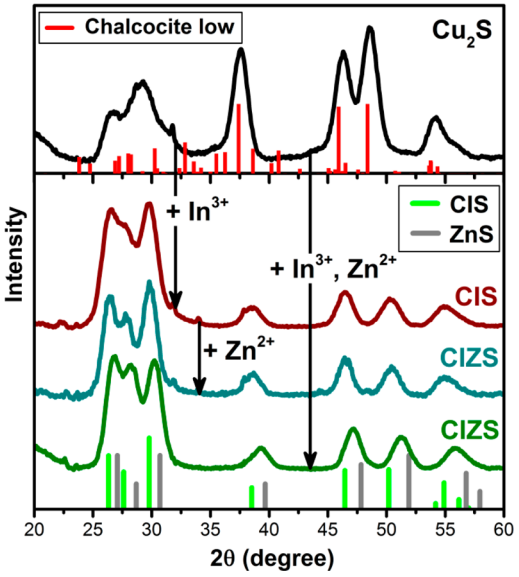


**Figure 3. XRD patterns of pristine $Cu_2S$ NCs, exchanged CIS, and CIZS NCs obtained by sequential and simultaneous injection of indium and zinc precursors. The line diffraction patterns show the bulk $Cu_2S$ low chalcocite (ICSD card 23596), wurtzite ZnS (ICSD card 67453), and CIS (ICSD card 163489).**

indicating the preservation of their overall shape. The average size of the particles decreased from 7.9 ± 1.0 to 5.7 ± 1.3 nm and their size distribution broadened to a small degree, presumably due to the slight etching of the NCs by TOP. The In:Cu ratio in the resulting CIS NCs was determined by inductively coupled plasma optical emission spectroscopy (ICP-OES) and X-ray photoelectron spectroscopy (XPS) analyses and was found to be 0.41:0.59 on average (0.40:0.60 and 0.42:0.58 from ICP and XPS, respectively).

HRTEM and XRD observations were performed to further study the structural transformation of pristine $Cu_2S$ to CIS NCs during the exchange. As depicted in Figure 2d, the exchanged NCs exhibited the typical {100} and {110} lattice sets of a hexagonal symmetry, with measured *d*-spacing of 3.5 and 2.0 Å, respectively. The lattice parameters extracted from HRTEM data conform to a high chalcocite-like phase, as also shown by the FT analysis (see Figure 2f). By XRD analysis this crystal structure could be indexed as the metastable wurtzite $CuInS_2$ rather than the thermodynamically stable zincblende phase (see Figure 3). In this way, the wurtzite CIS can be derived by replacing $Zn^{2+}$ with $In^{3+}$ and $Cu^{+}$ ions in the cation sites of wurtzite ZnS crystal structure, as described by Pan *et al.*[44] In CE reactions, the anionic sublattice is often maintained, and therefore, it has a strong influence on the crystal structure of resulting exchanged NCs.[29,30,36] For example, as it has recently been shown for the complete CE of $Cu_2S$ nanoparticles toward ZnS, the initial hexagonal crystal structure was preserved,[35] most probably due to very similar ionic radii of $Cu^{+}$ and $Zn^{2+}$ having the same coordination numbers.[45] The same

**TABLE 1. Composition Control of CIS NCs**

| parameter | In:Cu molar ratio in NCs |
|---|---|
| Reaction Time,[a] min | |
| 5 | 0.28:0.72 |
| 15 | 0.40:0.60 |
| 30 | 0.45:0.55 |
| Initial In:Cu Precursor Molar Ratio[b] | |
| 0.1 | 0.02:0.98 |
| 0.2 | 0.07:0.93 |
| 0.5 | 0.28:0.72 |
| 1 | 0.44:0.56 |
| $Cu_2S$ NC size,[c] nm | |
| 3.7 | 0.42:0.58 |
| 4.5 | 0.42:0.58 |
| 5.2 | 0.42:0.58 |
| 7.9 | 0.40:0.60 |

[a] CE performed on 7.9 nm $Cu_2S$ NCs with an initial precursor molar ratio of In:Cu = 0.5. [b] CE on 7.9 nm $Cu_2S$ NCs, reaction time = 5 min. [c] Reaction time = 15 min, an initial ratio In:Cu = 0.5.

is applicable to the pair $In^{3+}/Cu^{+}$ ions, also exhibiting similar ionic radii of 0.62 and 0.6 Å for tetrahedral coordination and 0.8 and 0.77 Å for octahedral coordination, respectively.[45] In our case low symmetry monoclinic crystal structure of pristine $Cu_2S$ particles underwent a slight rearrangement to higher symmetry hexagonal lattice of CIS NCs. As Table 1 indicates, the In:Cu ratio in CIS NCs could be finely tuned by varying both the initial ratio between $In^{3+}$ precursor and the amount of $Cu^{+}$ in NCs, and the exchange reaction time. Both approaches provide a significant control over the stoichiometry of the resulting particles. Thus, already 5 min after the reaction start at 120 °C $In^{3+}$ replaces almost 30% of copper ions in the parent $Cu_2S$ NCs. By extending the exchange time to 30 min, it is possible to replace ~45% of copper. Increasing the indium precursor concentration in the reaction mixture also leads to the increment of incorporated $In^{3+}$ ions. Thus, using 10-fold excess of the indium precursor, as compared to copper, it is possible to replace over 60% of $Cu^{+}$ ions. Furthermore, differently sized pristine $Cu_2S$ NCs (3.7−7.8 nm) were used as seeds for the synthesis of CIS NCs. As seen from Table 1, within this size range there is no remarkable difference in the indium incorporation efficiency owing to a homogeneous alloying.

**Synthesis of CIZS NCs: $Zn^{2+}$ Incorporation.** As recently demonstrated by our group, the incorporation of $Zn^{2+}$ ions into CIS NCs dramatically enhances PL efficiency of the resulting material.[16] Therefore, as a next step after $Cu^{+} \rightarrow In^{3+}$ partial exchange yielding CIS NCs, we performed a second partial CE reaction with the incorporation of zinc, similar to the method reported by Zhang *et al.*[19] In this approach, the zinc precursor was injected at 100 °C in the crude reaction mixture right after $Cu^{+} \rightarrow In^{3+}$ exchange. We note that the addition of octylamine (OctAm) by preparation of a Zn precursor

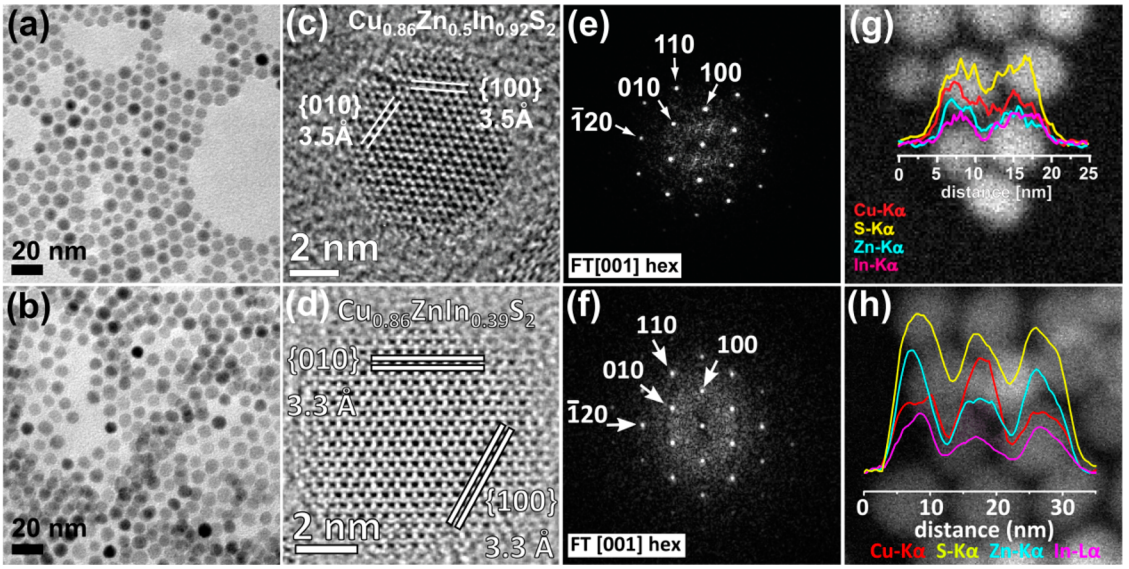


**Figure 4. Conventional TEM images of CIZS NCs obtained by sequential (a) and combined (b) CE. (c, d) HRTEM characterization of the corresponding NCs displaying their main lattice sets. (e, f) Corresponding FT patterns consistent with [001] zone axis projections of high chalcocite-like structure. STEM-EDS line profiles display the distribution of elements (Cu, Zn, In, S) across CIZS NCs obtained by sequential (g) and combined (h) CE.**

improves solubilization of the zinc salt yielding stable solutions without formation of gels, as has been observed by using solely OlAm as a ligand. The temperature of the reaction has been kept at 100 °C to prevent diffusion of $Zn^{2+}$ into the core of the CIS NCs. As depicted in Figure 4a, the shape of the CIS NCs was preserved after the zinc incorporation, although the average size increased from 5.7 ± 1.3 nm of CIS NCs to 6.5 ± 1.3 nm. The obtained CIZS NCs had a Cu:In:Zn:S ratio of 0.86:0.92:0.5:2 according to STEM-EDS data.

HRTEM observations and FT analysis evidenced that the chalcocite-like crystal structure of the initial $Cu_2S$ NCs and CIS particles synthesized thereof, was preserved also after Zn incorporation. CIZS NCs exhibited the typical {100} and {110} lattice sets of the hexagonal structure, with measured *d*-spacing of 3.5 and 2 Å, respectively (see Figure 4c,e). These lattice parameters are equal to those of CIS NCs. STEM-EDS line profile analysis indicated the alloy nature of CIZS NCs, revealing that no core/shell, or janus structures were formed as a result of CE (see Figure 4g). In contrast to the $Cu^+ \rightarrow In^{3+}$ exchange, the incorporated amount of Zn is limited for larger 7.9 nm CIZS NCs (see Table 2). With both prolonged reaction time and increased initial Zn:Cu ratio, only a maximum of Zn:(Cu + In) = 0.17:0.83 could be achieved. Furthermore, after the reaction the In:Cu ratio dropped by 10% from the parent CIS NCs to the CIZS NCs, indicating a more favorable exchange of $Zn^{2+}$ with $In^{3+}$, rather than with $Cu^+$. This was also confirmed by XPS results (discussed below).

When the CE reactions on the 7.9 nm $Cu_2S$ NCs were combined ($Cu^+ \rightarrow In^{3+}$, $Zn^{2+}$) instead of following the sequential approach, the Zn:(Cu + In) ratio could be sufficiently boosted owing to an increase of the reactivity of the Zn precursor at a higher temperature (120 °C *vs* 100 °C). We note that at 100 °C we did not observe any incorporation of $In^{3+}$. Hence, these reaction conditions favor the incorporation of zinc, and thus for an efficient indium incorporation, the Zn precursor should be used in a lower amount than In, as follows from Table 3. As in the case of sequentially exchanged CIZS NCs, HRTEM and FT analyses revealed the typical {100} and {110} lattice sets of hexagonal structure, with measured *d*-spacing of 3.3 and 1.9 Å, respectively (see Figure 4d,f). The lattice parameters extracted from HRTEM data are consistent with a high

**TABLE 2. Composition Control of CIZS NCs Obtained from CIS NCs**

| | molar ratio in NCs | | |
|---|---|---|---|
| parameter | Zn:(Cu + In) | Zn:Cu | In:Cu |
| | Reaction Time,[a] min | | |
| 10 | 0.05:0.95 | 0.09:0.91 | 0.55:0.45 |
| 30 | 0.11:0.89 | 0.22:0.78 | 0.57:0.43 |
| 60 | 0.12:0.88 | 0.22:0.78 | 0.58:0.42 |
| | Initial Zn:Cu Precursor Molar Ratio[b] | | |
| 1 | 0.11:0.89 | 0.22:0.78 | 0.57:0.43 |
| 4 | 0.17:0.83 | 0.25:0.75 | 0.38:0.62 |
| | $Cu_2S$ NC size,[c] nm | | |
| 3.7 | 0.47:0.53 | 0.57:0.43 | 0.32:0.68 (0.42:0.58)[d] |
| 4.5 | 0.28:0.72 | 0.40:0.60 | 0.43:0.57 (0.42:0.58)[e] |
| 5.2 | 0.17:0.83 | 0.26:0.74 | 0.40:0.60 (0.37:0.63)[f] |
| 7.9 | 0.11:0.89 | 0.22:0.78 | 0.57:0.43 (0.52:0.48)[g] |

[a] CE performed on 5.7 nm CIS NCs with an initial precursor molar ratio of Zn:Cu = 1. In:Cu in initial CIS NCs = 1.08. [b] CE on 5.7 nm CIS NCs, reaction time = 30 min. In:Cu in initial CIS NCs = 1.08. [c] Reaction time = 30 min, an initial precursor ratio Zn:Cu = 1. [d–g] Initial In:Cu ratio in CIS NCs.

chalcocite-like phase, as shown by the FT pattern consistent with the [001] zone axis projection of high chalcocite (Figure 4f). Due to a larger amount of incorporated zinc ions, the XRD peaks shifted to higher 2-$\theta$ angles toward the peaks of wurtzite ZnS, occupying an intermediate 2-$\theta$ position between diffraction lines of CIS and ZnS patterns, as shown in Figure 3.

In order to further study the structure of the synthesized NCs, we have characterized them by XPS, since this technique is known to be mainly sensitive to the surface of nanoparticles. As follows from the data analysis, in CIS NCs the ratio In:Cu = 0.42:0.58 (see Figure SI5, Supporting Information) is in agreement with that determined by ICP (0.40:0.60), implying some deviations of element distributions from a perfectly homogeneous alloy; *i.e.*, the NC shell is richer in indium than the core. Furthermore, we have observed prominent differences in the composition of the surface of CIZS NCs prepared *via* sequential and combined CE. As depicted in Figure 5, Zn 2p peaks of CIZS NCs synthesized by a combined exchange exhibit intensity higher than those of the sequentially exchanged sample, both normalized with respect to copper signal taken as a reference. At the same time, indium lines are more prominent in CIZS-seq NCs. Quantification of the data gives Cu:In:Zn ratios of 0.46:0.29:0.25 and 0.34:0.09:0.57 for sequential and combined samples, respectively. As compared to the ICP data (Cu:In:Zn ratios of 0.52:0.38:0.10 and 0.31:0.12:0.57 for sequential and combined samples, respectively), XPS indicated a much higher Zn content compared to ICP for the CIZS-seq samples, whereas CIZS-comb particles do not exhibit a significant deviation between the ICP and XPS data sets. These findings reveal that by sequential exchange Zn tends to replace Cu and In mostly on the surface of NCs, while simultaneous incorporation leads to a more homogeneous distribution of guest cations within the particles.

As mentioned above, according to our results, the amount of zinc incorporated in sequential exchange is much lower than that achieved *via* combined reaction. This suggests that incorporation of indium in copper sulfide NCs makes them more rigid toward further exchange and prevents intercalation of Zn at a moderate temperature. As shown by Groeneveld *et al.*, CE reactions at low temperatures are usually limited due to the limited available Frenkel pairs,[46] leading to the formation of ZnS monolayer or a very thin ZnS-rich layer, which is not detectable by STEM-EDS mapping. Hence, extended reaction times and higher concentrations of guest cations should not influence strongly the Zn:(Cu + In) ratio in NCs. This assumption is further supported when smaller sized CIS NCs were used as seeds. Whereas the size of the parent $Cu_2S$ NCs did not

**TABLE 3. Composition Control of CIZS NCs Obtained from $Cu_2S$ NCs by Combined CE[a]**

| Cu:In:Zn ratio in reaction mixture | Cu:In:Zn ratio in NCs |
|---|---|
| 0.44:0.44:0.12 | 0.43:0.16:0.41 |
| 0.31:0.61:0.08 | 0.42:0.48:0.1 |
| 0.47:0.47:0.06 | 0.37:0.49:0.14 |

[a] Performed on 7.9 nm $Cu_2S$ NCs, reaction temperature = 120 °C, reaction time = 20 min.

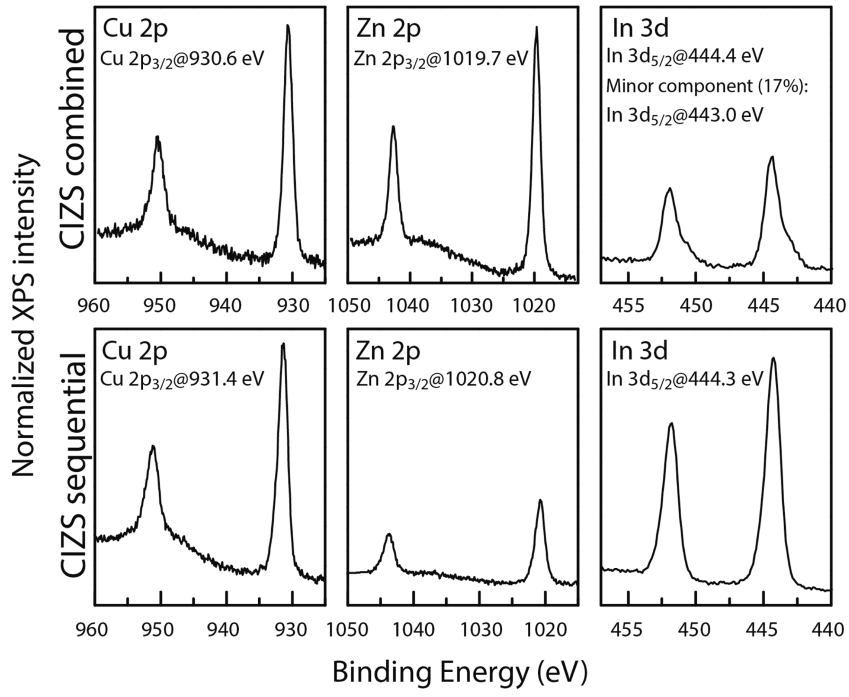


**Figure 5. XPS narrow scans on Cu 2p, Zn 2p and In 3d peaks of CIZS NCs synthesized by combined (top panel) and sequential (bottom panel) CE reactions.**

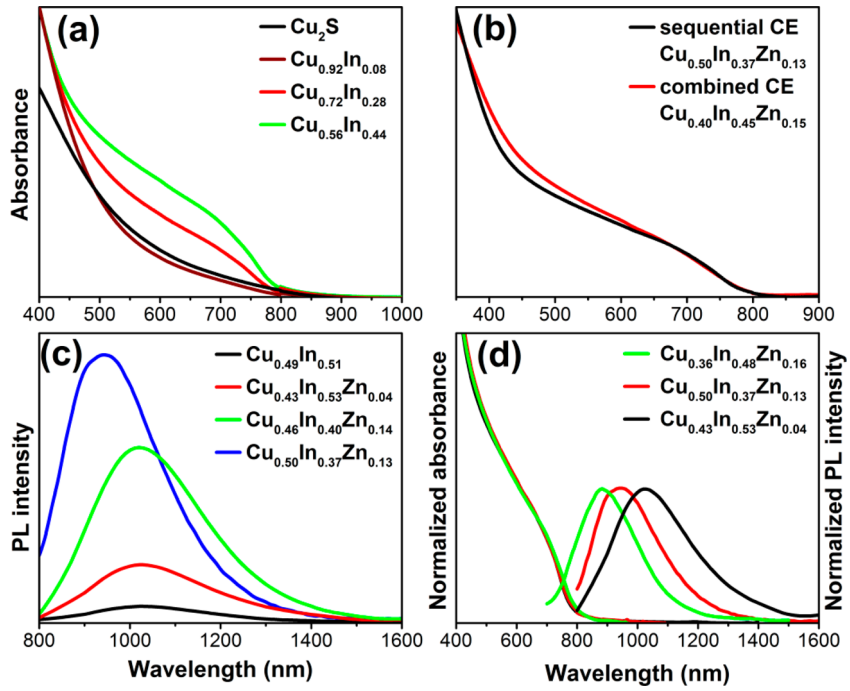


**Figure 6. (a) Absorption spectra of parent $Cu_2S$ NCs and exchanged CIS NCs with varied In content. (b) Absorption spectra of CIZS NCs obtained by sequential and combined CE. (c) PL spectra of CIZS NCs with increasing Zn content. (d) Absorption and PL spectra of CIZS NCs with different compositions.**

remarkably affect the incorporation of $In^{3+}$, the size of CIS does strongly influence the incorporation of $Zn^{2+}$. With decreasing size from 7.8 to 3.7 nm, the Zn:(Cu + In) ratio could be increased from 0.12:0.88 to 0.49:0.51. This again reveals the formation of a ZnS-rich shell with a certain thickness, which with decreasing size consequently constitutes a larger part of the particle, since $Zn^{2+}$ replaces a relatively larger number of $Cu^{+}$ and $In^{3+}$ ions accessible on the surface.

**Optical Properties of $Cu_2S$, CIS, and CIZS NCs.** Analysis of UV−vis−NIR optical spectra of pristine and exchanged NCs, presented in Figure 6, confirms the conclusions reached based on the structural characterization and yields a more detailed view on the band-edge and vacancy-assisted absorption and emission, respectively. As follows from Figure 6a, incorporation of $In^{3+}$ ions into parent copper sulfide particles leads to the development of a prominent absorption band around ~700 nm, which intensifies by increasing the indium content. This feature remains practically unaltered by following incorporation of $Zn^{2+}$ ions, as seen in Figure 6b. By this, the shape of the spectral profile practically does not depend on which CE procedure is followed, that is, whether combined or sequential. As we discussed above, by the sequential exchange $Zn^{2+}$ ions replace both $In^{3+}$ and $Cu^{+}$ ions in CIS NCs forming a ZnS-rich surface. This leads to a sufficient enhancement of the PL intensity (see Figure SI6, Supporting Information) and to a blue shift of the PL maximum from ~1030 nm for a weakly emitting CIS NC sample to 940 nm for $Cu_{0.5}In_{0.37}Zn_{0.13}$ NC sample (see Figure 6c). Here we note that in order to increase the PL intensity of CIZS NCs, they were treated at elevated temperatures (up to 200 °C) right after the Zn exchange, which presumably yields a more complete ZnS shell, as in the case of $Cu_{0.46}In_{0.4}Zn_{0.14}$ and $Cu_{0.5}In_{0.37}Zn_{0.13}$ NC samples annealed at 150 and 200 °C, respectively. At the same time, the variation of zinc content in CIZS NCs does not lead to a prominent change in absorption spectra of the samples, as presented in Figure 6d. This allows us to tune PL from 880 to 1025 nm without altering the optical absorption. PL measurements provide us an additional proof of the NC surface passivation with ZnS-rich layer in the case of sequential CE, since NCs obtained by the combined exchange do not exhibit any emission. Absolute quantum efficiencies of the NIR-emitting NC samples remained quite low, however, for instance about 1% for $Cu_{0.5}In_{0.37}Zn_{0.13}$ NC sample.

**Cyclic Voltammetry.** We have carried out cyclic voltammetry analysis (CV) of our NCs in order to gain insight into their energy levels and to estimate their electrochemical band gaps ($E_{g,EC}$).[42,47,48] Basically, CV imposes a potential sweep ($V$) on working electrodes (NCs) and measures their response in terms of the current ($I$) related to their red−ox processes.[49] In principle, the onset of red−ox processes in semiconductor NCs can be related to the edges of valence and conduction bands upon charge transfer ($e^{-}/h^{+}$).[50,51] Figure 7 reports the CV data of the NCs, evidencing the characteristic gap or energy barrier in the middle of potential scan followed by asymmetric red−ox peaks (potentials are reported *vs* Ag/AgCl). We note that the oxidation/reduction peaks

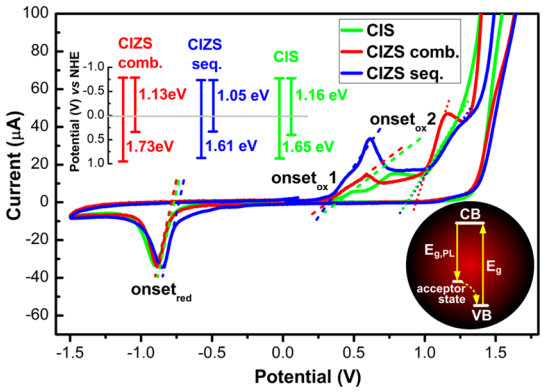


**Figure 7. CV traces of CIS and CIZS NCs synthesized by sequential and combined CE reactions (potentials are reported *vs* Ag/AgCl). The top left inset reports electrochemical band gap values and energy gaps between conduction bands and acceptor states deduced from corresponding CV curves (potentials are reported *vs* NHE). The bottom right inset displays a sketch of a possible exciton relaxation pathway in a CIS or CIZS NC, where $E_g$ corresponds to an optical or electrochemical band gap and $E_{g,PL}$ corresponds to a gap between conduction band and an acceptor state responsible for PL properties.**

of the NCs appear at slightly different potentials, signifying the variation in their chemical composition and structure. Furthermore, while all CV curves in Figure 7 clearly exhibit one reduction peak at about −0.87 V with corresponding onset at about −0.76 V, two types of oxidation peaks can be identified. Onsets of the first set of the peaks lie in the range of 0.3−0.4 V ($onset_{ox}1$), whereas the second type peaks are less prominent but have larger current values, their onsets extrapolated to the range of 0.87−0.94 V ($onset_{ox}2$). By combining these data with results of optical absorption and emission spectroscopy presented in Figure 6, we may attribute the most intensive oxidation peaks to the addition of holes to the valence bands of NCs and thus estimate their $E_{g,EC}$ as the gap between onsets of oxidation and reduction peaks, which are presented as an inset in Figure 7 (top left, potentials are reported *vs* NHE). As follows from the comparison with optical absorption data, these values are in a good agreement, *i.e.*, absorption band at ∼700 nm and $E_{g,EC}$ bands in the range of 1.61−1.73 eV, corresponding to ∼720−770 nm.

Following this analysis, we can ascribe the first set of oxidation peaks to the positions of intrinsic acceptor states such as Cu vacancies and interstitial $In^{3+}$ or/and $Zn^{2+}$ ions, which serve as deep traps for exciton recombination and hence are responsible for light emission properties of the NCs (see bottom right inset in Figure 7). Indeed, the gaps derived from reduction onsets and onsets of the first peaks correspond well to the PL data of the CIS, CIZS NCs: 1.05−1.16 eV (1070−1180 nm) *vs* approximately 900−1030 nm of the PL maxima positions. Hence, while the absorption in CIS and CIZS NCs does not vary significantly with the overall NC composition, the Stokes shift between the band-edge absorption and the trap-assisted PL can be carefully controlled by the stoichiometry, *i.e.*, the concentration and local environment of the deep acceptor states. Note that although CIZS-comb NCs exhibit a well resolved first oxidation peak indicating the presence of acceptor states, they are nonfluorescent, most probably due to surface trap states which are not passivated by a ZnS shell. In addition, the CV curve of the initial $Cu_2S$ NCs (see Figure SI7, Supporting Information) also shows an oxidation peak of low intensity at ∼0.3 V (position similar to $onset_{ox}1$ of CIS and CIZS NCs), implying the presence of a small number of Cu vacancies, that actually was confirmed by HRTEM analysis (see Figure 2) which gave a composition of $Cu_{1.96}S$ (*i.e.*, $x = 0.04$ in $Cu_{2-x}S$).

**Biocompatibility of CIZS NCs.** In order to verify the potential applicability of the synthesized core/shell-like CIZS NCs as biolabeling probes, thiol-pegylated molecules (molecular weight = 2000 KDa) were used for the phase transfer to water. Cytotoxicity of these stable PEG-coated CIZS NCs was assessed using two different cell cultures, *i.e.*, KB cells (human epidermal carcinoma) and A549 cells (human alveolar adenocarcinoma). As shown in Figure SI8 (in the Supporting Information), while the KB cells exhibited no toxicity for almost all tested concentrations of CIZS nanoparticles, the A549 cells were slightly more sensitive to the NCs, though the cell viability was always higher than 80%. These results allow us to consider the material as having a low toxicity even at the highest concentration of NCs tested (85 nM). Comparison with literature proliferation data on NCs having a similar composition, but prepared by different synthesis routes and transferred into water by encapsulation into an amphiphilic polymer shell, showed that in our proliferation assay we used a much higher NC dose (20 μg/mL of Cu *vs* 0.05 μg/mL from the previous work) with a still small toxicity effect (less than 20% in terms of cell mortality).[38] These data confirm a sufficient biocompatibility of CIZS NCs, making them a safer probe than Cd-containing quantum dots for *in vivo* biological tracking studies.[23]

## CONCLUSION

We have developed a method for the synthesis of CIS and CIZS NCs by using a three-step approach based on a partial cation exchange, starting from $Cu_2S$ nanoparticles. In the first step, $Cu_2S$ NCs were synthesized, followed by the partial cation exchange in which $In^{3+}$ replaced $Cu^{+}$. The shape of the particles after the $In^{3+}$ incorporation was preserved, although it was accompanied by a small decrease in size. Furthermore, the In:Cu ratio could be well controlled by varying the reaction time as well as the ratio between In-precursor and Cu in NCs. Sequentially, $Zn^{2+}$ ions were introduced and formed core/shell-like alloy CIZS/ZnS NCs. Furthermore, it was shown that by combining two precursors ($In^{3+}$ and $Zn^{2+}$) in one pot, homogeneously

alloyed CIZS NCs with higher zinc content could be synthesized. Moreover, we have demonstrated that the sequential exchange with $Zn^{2+}$ leads to a sufficient increase of the PL efficiency and that PL could be tuned from 850 to 1030 nm by carefully controlling the Cu:In:Zn content in the NCs. Combination of optical characterization with cyclic voltammetry results provides a further insight into the electronic structure of the NCs, namely their band gap values lying within 1.61−1.73 eV as well as relative positions of intrinsic acceptor energy levels which determine photoluminescence properties of CIS and CIZS NCs. Finally, the core/shell CIZS NCs were transferred in water by ligand exchange to hydrophilic thiol-containing polyethylene glycol molecules and their cytotoxicity was tested on KB and A549 cells indicating their biocompatibility.

## EXPERIMENTAL SECTION

**Materials.** Indium(III) acetylacetonate ($In(acac)_3$, 99.99%), zinc acetate ($Zn(OAc)_2$, 99.99%), copper(II) acetylacetonate ($Cu(acac)_2$, 99.99%), thiourea (99%), octadecene (ODE, technical grade, 90%), 1-dodecanethiol (DDT, ≥98%), octylamine (OctAm, 99%), oleylamine (OlAm, 70%), tetrachloroethylene (TCE, ≥99%), tetrabutylammonium hexafluorophosphate (TBAPF6, ≥99%), acetonitrile (99.8%), anhydrous methanol (99.9%), hexane (95%), and chloroform ($CHCl_3$, ≥99.95%) were purchased from Sigma-Aldrich. Tri-*n*-octylphosphine (TOP, 97%) was purchased from STREM chemicals, $CH_3O$-PEG-SH polymer ($M_w$ = 2000) was purchased from RAPP Polymere GmbH. All chemicals were used without any further purification, except for OlAm, OctAm, and ODE, which were degassed at 100 °C for 2 h in vacuum prior to the synthesis.

**Synthesis of Parent $Cu_2S$ NCs.** In a typical synthesis, a mixture of 131 mg of $Cu(acac)_2$ (0.5 mmol), 19 mg of thiourea (0.25 mmol), 5 mL of OlAm, and 2.5 mL of DDT was degassed in a three-neck flask under vacuum for 30 min at 70 °C. After degassing, the flask was filled with nitrogen and the temperature was raised to 170 °C within 4 min. The solution was maintained at this temperature for 30 min with subsequent cooling to 120 °C for further synthesis of the CIS NCs (see the following section). For the characterization of $Cu_2S$ NCs an aliquot of the reaction mixture was cooled to room temperature and was cleaned by repeated precipitation with methanol and redispersion in $CHCl_3$ for three times.

**Synthesis of CIS NCs.** When the reaction mixture, as described in the previous section, was cooled to 120 °C, a solution of 103 mg $In(acac)_3$ (0.25 mmol) in 8 mL of ODE and 2 mL of TOP (previously degassed in a glovebox at ∼180 °C) was swiftly injected. The temperature was maintained at 120 °C for 15 min. Finally, the solution was cooled to 100 °C for further zinc incorporation. For the various characterizations, CIS NCs were purified analogous to $Cu_2S$ NCs.

**Synthesis of CIZS NCs.** After the crude CIS NC solution was cooled to 100 °C, a mixture of 91 mg of $Zn(OAc)_2$ (0.5 mmol) in 0.9 mL of ODE, 0.1 mL of OlAm, and 0.1 mL of OctAm (previously degassed in a glovebox at ∼180 °C) was swiftly injected. The reaction was kept for 30 min at 100 °C followed by cooling to room temperature.

**Synthesis of CIZS NCs by Simultaneous Cation Exchange.** Alternatively, CIZS NCs were prepared by a simultaneous injection of $In^{3+}$ and $Zn^{2+}$ precursors into the crude $Cu_2S$ NC solution after its cooling to 120 °C. In this reaction mixture, a solution of 23 mg of $Zn(OAc)_2$ (0.125 mmol) and 206 mg of $In(acac)_3$ (0.5 mmol) in 0.4 mL of OlAm, 0.4 mL of OctAm, 1 mL of ODE, and 2 mL TOP (previously degassed in a glovebox at ∼180 °C) was swiftly injected. The temperature was maintained at 120 °C for 20 min. For the NC cleaning, the same procedure as for $Cu_2S$ and CIS was employed.

**Water Transfer of CIZS NCs by Polymer Coating.** To transfer the as-prepared CIZS NCs in water, 0.5 mL of cleaned CIZS NC (6.5 nm size) solution was redispersed in 5 mL of hexane and swiftly added to 225 mg of $CH_3O$-PEG-SH polymer (approximately 200 times weight excess as compared to the NCs content) dissolved in 5 mL of methanol followed by overnight shaking. After the incubation time, the methanol phase became colored, indicating the migration of NCs. Then, the methanol phase was separated and the NCs were completely dried with subsequent addition of 5 mL water. Finally, to remove the unbound PEG molecules, the CIZS NCs were centrifuged three times in filter centrifugation tubes at 4000 rpm for 5 min and redispersed in water.

**Transmission Electron Microscopy (TEM).** Conventional TEM observations were carried out using a JEOL JEM 1011 microscope equipped with a thermionic gun operating at 100 kV of accelerating voltage. High-resolution TEM (HRTEM) imaging was performed on a JEOL JEM-2200FS microscope equipped with a field emission gun working at an accelerating voltage of 200 kV, a CEOS spherical aberration corrector of objective lens allowing to reach a spatial resolution of 0.9 Å, and an in column Omega filter. The chemical composition of the NCs was determined by energy dispersive X-ray spectroscopy (EDS) analysis performed in high angle annular dark field scanning TEM (HAADF-STEM) mode with a 0.7 nm electron probe and a Bruker Quantax 400 system with a 60 $mm^2$ XFlash 6T silicon drift detector, using the Cliff-Lorimer method. STEM-EDS measurements were carried out using an analytical double tilt holder equipped with a low background beryllium tip in order to avoid any interference between the signals coming from the grid/holder and the NCs. Samples were prepared by dropping diluted NC colloidal suspensions onto carbon-coated 200 mesh copper and aluminum grids for conventional TEM and HRTEM imaging, respectively, with subsequent solvent evaporation.

**Scanning Electron Microscopy-Energy Dispersive X-ray Spectroscopy (SEM-EDS).** Additional EDS analysis was performed on a high-resolution scanning electron microscope JEOL JSM-7500F equipped with a cold field emission gun using an Oxford X-Max 80 system with a silicon drift detector having an 80 $mm^2$ effective area. The analyses were done with an accelerating voltage of 10 kV, and the spectra were acquired for 300 s live time. Standardless quantification was achieved with Aztec Energy EDS Software.

**Powder X-ray Diffraction (XRD) Analysis.** For the XRD analysis, a Rigaku SmartLab 9 kW diffractometer was used with a Cu source operating at 40 kV and 150 mA. A Göbel mirror was used to obtain a parallel beam and to suppress Cu K$\beta$ radiation (1.392 Å). Samples were prepared by drop casting concentrated NC solutions on a zero background silicon wafer.

**X-ray Photoelectron Spectroscopy (XPS).** Samples for XPS were prepared in a glovebox by drop-casting NC colloids on a graphite substrate (HOPG, ZYB quality, NT-MDT) and then transferred to the XPS setup avoiding air-exposure. Measurements were performed on a Kratos Axis Ultra DLD spectrometer, using a monochromatic Al K$\alpha$ source (15 kV, 20 mA). Wide scans were acquired at analyzer pass energy of 160 eV. High resolution narrow scans were performed at constant pass energy of 10 eV and steps of 0.1 eV. The photoelectrons were detected at a takeoff angle of $\Phi = 0°$ with respect to the surface normal. The pressure in the analysis chamber was maintained below $7 \times 10^{-9}$ Torr for data acquisition. The data were converted to VAMAS format and processed using CasaXPS software, version 2.3.15. The binding energy (BE) scale was internally referenced to the C 1s peak (BE for C−C = 284.8 eV).

**UV−vis−NIR Absorption Spectroscopy.** Absorbance spectra were measured on a Varian Cary 5000 UV−vis−NIR spectrophotometer. The NC solutions were prepared by redispersing the NCs into 1 mL of TCE in 1 cm path length quartz cuvettes. The sample preparation was performed inside a nitrogen-filled glovebox.

**PL Measurements.** NCs were dispersed in TCE at an optical density of about 0.1−0.2 $cm^{-1}$ at the excitation wavelength. The steady-state PL spectra were collected with an Edinburgh Instruments FLS920 spectrofluoremeter, by exciting the samples at 400 nm using a Xe lamp coupled to a monochromator. The PL quantum efficiency was determined with an integrating sphere by exciting CIZS NC colloids at 700 nm.

**Cyclic Voltammetry.** Electrochemical measurements were carried out in a conventional three-electrode glass cell using a PARSTAT 2273. An electrolyte solution containing TBAPF6 (0.1 M) in acetonitrile was purged with nitrogen prior to the measurements for removing the traces of oxygen. The glassy carbon disk electrodes used in experiments were polished to a mirror-like finish with a diamond paste (0.5 $\mu$m particles) and repeatedly washed with acetone and ethanol. NCs from solution were then directly drop-casted onto the glassy carbon electrodes and allowed to dry in a nitrogen-filled glovebox. All potentials were reported *vs* Ag/AgCl, and for the band gap estimation the potentials were reported *vs* NHE.

**Cytotoxicity Assay.** To investigate the biocompatibility of CIZS NCs, cytotoxicity assays were performed with KB cells (human epidermal carcinoma) and A549 cells (human alveolar adenocarcinoma). $10^4$ cells suspended in 1 mL of medium (RPMI 1640 for KB, DMEM for A549) supplemented with 10% FBS were seeded in a 96-multiwell plate. After their incubation for 24 h at 37 °C and 5% of $CO_2$, the medium was replaced with 1 mL of the fresh medium containing different concentrations of NCs. After 96 h of the treatment the medium was removed, the cells were washed three times with PBS, and 1 mL of fresh serum-free medium containing PrestoBlue (Life Technologies) was added into each well. After 20 min of incubation at 37 °C, the medium was transferred in a new, empty 96-multiwell plate, and optical absorption at 570 nm was recorded on a Multiskan GO microplate spectrophotometer (Thermo Scientific) by subtracting absorption of blank samples (the signal measured on the cell medium only). All values measured were compared to untreated control samples. The assay was repeated at least three times for each experimental point.

**Elemental Analysis.** Inductively coupled plasma optical emission spectroscopy (ICP-OES) analysis performed on an iCAP 6000 spectrometer (ThermoScientific) was used to quantify the copper, indium, and zinc content in the NCs. Prior to measurements, the samples were decomposed in aqua regia ($HCl/HNO_3$ = 3/1 (v/v)) overnight.

*Conflict of Interest:* The authors declare no competing financial interest.

*Supporting Information Available:* TEM images of differently sized, self-assembled $Cu_2S$ NCs as well as $Cu_2S$ nanodisks. HAADF-STEM images of $Cu_2S$, CIS, CIZS-seq, and CIZS-comb NCs. XPS spectra of CIS NCs. Photograph of nonemitting CIS and fluorescent CIZS NC solutions. CV curve of $Cu_2S$ NCs. Figure displaying results of the cytotoxicity test of CIZS NCs. This material is available free of charge *via* the Internet at http://pubs.acs.org.

*Acknowledgment.* We are grateful to Giammarino Pugliese for help with the water transfer of the NCs. Q.A.A. acknowledges support by the Erasmus Programme 2013−2014. V.L. acknowledges support by a Marie Curie Intra European Fellowship within the 7th European Community Framework Programme (FP7/2007-2013) under Grant Agreement No. 301100 (project "LOTOCON"). The research leading to these results has also received funding from the FP7 under Grant Agreement Nos. 614897 (ERC Consolidator Grant "TRANS-NANO") and 284486 (project "SCALENANO").

## REFERENCES AND NOTES

1. Talapin, D. V.; Lee, J.-S.; Kovalenko, M. V.; Shevchenko, E. V. Prospects of Colloidal Nanocrystals for Electronic and Optoelectronic Applications. *Chem. Rev.* **2010**, *110*, 389–458.
2. Kim, S.; Lim, Y. T.; Soltesz, E. G.; De Grand, A. M.; Lee, J.; Nakayama, A.; Parker, J. A.; Mihaljevic, T.; Laurence, R. G.; Dor, D. M.; *et al.* Near-Infrared Fluorescent Type II Quantum Dots for Sentinel Lymph Node Mapping. *Nat. Biotechnol.* **2004**, *22*, 93–97.
3. Sun, L.; Choi, J. J.; Stachnik, D.; Bartnik, A. C.; Hyun, B.-R.; Malliaras, G. G.; Hanrath, T.; Wise, F. W. Bright Infrared Quantum-Dot Light-Emitting Diodes Through Inter-Dot Spacing Control. *Nat. Nanotechnol.* **2012**, *7*, 369–373.
4. Tang, J.; Kemp, K. W.; Hoogland, S.; Jeong, K. S.; Liu, H.; Levina, L.; Furukawa, M.; Wang, X.; Debnath, R.; Cha, D.; *et al.* Colloidal-Quantum-Dot Photovoltaics Using Atomic-Ligand Passivation. *Nat. Mater.* **2011**, *10*, 765–771.
5. Song, W.-S.; Yang, H. Efficient White-Light-Emitting Diodes Fabricated from Highly Fluorescent Copper Indium Sulfide Core/Shell Quantum Dots. *Chem. Mater.* **2012**, *24*, 1961–1967.
6. Medintz, I. L.; Uyeda, H. T.; Goldman, E. R.; Mattoussi, H. Quantum Dot Bioconjugates for Imaging, Labelling and Sensing. *Nat. Mater.* **2005**, *4*, 435–446.
7. Choi, J.; Kang, N.; Yang, H. Y.; Kim, H. J.; Son, S. U. Colloidal Synthesis of Cubic-Phase Copper Selenide Nanodiscs and Their Optoelectronic Properties. *Chem. Mater.* **2010**, *22*, 3586–3588.
8. Wang, Y.; Hu, Y.; Zhang, Q.; Ge, J.; Lu, Z.; Hou, Y.; Yin, Y. One-Pot Synthesis and Optical Property of Copper(I) Sulfide Nanodisks. *Inorg. Chem.* **2010**, *49*, 6601–6608.
9. van der Stam, W.; Akkerman, Q. A.; Ke, X.; van Huis, M. A.; Bals, S.; de Mello Donega, C. Solution-Processable Ultrathin Size- and Shape-Controlled Colloidal $Cu_{2-x}S$ Nanosheets. *Chem. Mater.* **2014**, 10.1021/cm503929q.
10. Saldanha, P. L.; Brescia, R.; Prato, M.; Li, H.; Povia, M.; Manna, L.; Lesnyak, V. Generalized One-Pot Synthesis of Copper Sulfide, Selenide-Sulfide, and Telluride-Sulfide Nanoparticles. *Chem. Mater.* **2014**, *26*, 1442–1449.
11. Kolny-Olesiak, J.; Weller, H. Synthesis and Application of Colloidal $CuInS_2$ Semiconductor Nanocrystals. *ACS Appl. Mater. Interfaces* **2013**, *5*, 12221–12237.
12. Torimoto, T.; Adachi, T.; Okazaki, K. I.; Sakuraoka, M.; Shibayama, T.; Ohtani, B.; Kudo, A.; Kuwabata, S. Facile Synthesis of ZnS−$AgInS_2$ Solid Solution Nanoparticles for a Color-Adjustable Luminophore. *J. Am. Chem. Soc.* **2007**, *129*, 12388–12389.
13. Aldakov, D.; Lefrancois, A.; Reiss, P. Ternary and Quaternary Metal Chalcogenide Nanocrystals: Synthesis, Properties and Applications. *J. Mater. Chem. C* **2013**, *1*, 3756–3776.
14. Yarema, O.; Bozyigit, D.; Rousseau, I.; Nowack, L.; Yarema, M.; Heiss, W.; Wood, V. Highly Luminescent, Size- and Shape-Tunable Copper Indium Selenide Based Colloidal Nanocrystals. *Chem. Mater.* **2013**, *25*, 3753–3757.
15. Ramasamy, K.; Malik, M. A.; Revaprasadu, N.; O'Brien, P. Routes to Nanostructured Inorganic Materials with Potential for Solar Energy Applications. *Chem. Mater.* **2013**, *25*, 3551–3569.
16. De Trizio, L.; Prato, M.; Genovese, A.; Casu, A.; Povia, M.; Simonutti, R.; Alcocer, M. J. P.; D'Andrea, C.; Tassone, F.; Manna, L. Strongly Fluorescent Quaternary Cu−In−Zn−S Nanocrystals Prepared from $Cu_{1-x}InS_2$ Nanocrystals by Partial Cation Exchange. *Chem. Mater.* **2012**, *24*, 2400–2406.
17. Panthani, M. G.; Akhavan, V.; Goodfellow, B.; Schmidtke, J. P.; Dunn, L.; Dodabalapur, A.; Barbara, P. F.; Korgel, B. A. Synthesis of $CuInS_2$, $CuInSe_2$, and $Cu(In_xGa_{1-x})Se_2$ (CIGS) Nanocrystal "Inks" for Printable Photovoltaics. *J. Am. Chem. Soc.* **2008**, *130*, 16770–16777.
18. Chen, B.; Zhong, H.; Zhang, W.; Tan, Z. a.; Li, Y.; Yu, C.; Zhai, T.; Bando, Y.; Yang, S.; Zou, B. Highly Emissive and Color-Tunable $CuInS_2$-Based Colloidal Semiconductor Nanocrystals: Off-Stoichiometry Effects and Improved Electroluminescence Performance. *Adv. Funct. Mater.* **2012**, *22*, 2081–2088.
19. Zhang, W.; Lou, Q.; Ji, W.; Zhao, J.; Zhong, X. Color-Tunable Highly Bright Photoluminescence of Cadmium-Free Cu-Doped Zn−In−S Nanocrystals and Electroluminescence. *Chem. Mater.* **2014**, *26*, 1204–1212.
20. Chen, Y.; Li, S.; Huang, L.; Pan, D. Green and Facile Synthesis of Water-Soluble Cu−In−S/ZnS Core/Shell Quantum Dots. *Inorg. Chem.* **2013**, *52*, 7819–7821.

21. Li, L.; Pandey, A.; Werder, D. J.; Khanal, B. P.; Pietryga, J. M.; Klimov, V. I. Efficient Synthesis of Highly Luminescent Copper Indium Sulfide-Based Core/Shell Nanocrystals with Surprisingly Long-Lived Emission. *J. Am. Chem. Soc.* **2011**, *133*, 1176–1179.
22. Li, L.; Daou, T. J.; Texier, I.; Chi, T. T. K.; Liem, N. Q.; Reiss, P. Highly Luminescent $CuInS_2$/ZnS Core/Shell Nanocrystals: Cadmium-Free Quantum Dots for *In Vivo* Imaging. *Chem. Mater.* **2009**, *21*, 2422–2429.
23. Pons, T.; Pic, E.; Lequeux, N.; Cassette, E.; Bezdetnaya, L.; Guillemin, F.; Marchal, F.; Dubertret, B. Cadmium-Free $CuInS_2$/ZnS Quantum Dots for Sentinel Lymph Node Imaging with Reduced Toxicity. *ACS Nano* **2010**, *4*, 2531–2538.
24. Han, W.; Yi, L.; Zhao, N.; Tang, A.; Gao, M.; Tang, Z. Synthesis and Shape-Tailoring of Copper Sulfide/Indium Sulfide-Based Nanocrystals. *J. Am. Chem. Soc.* **2008**, *130*, 13152–13161.
25. Sarkar, S.; Karan, N. S.; Pradhan, N. Ultrasmall Color-Tunable Copper-Doped Ternary Semiconductor Nanocrystal Emitters. *Angew. Chem., Int. Ed.* **2011**, *50*, 6065–6069.
26. Norako, M. E.; Franzman, M. A.; Brutchey, R. L. Growth Kinetics of Monodisperse Cu-In-S Nanocrystals Using a Dialkyl Disulfide Sulfur Source. *Chem. Mater.* **2009**, *21*, 4299–4304.
27. Kuzuya, T.; Hamanaka, Y.; Itoh, K.; Kino, T.; Sumiyama, K.; Fukunaka, Y.; Hirai, S. Phase Control and Its Mechanism of $CuInS_2$ Nanoparticles. *J. Colloid Interface Sci.* **2012**, *388*, 137–143.
28. Li, H.; Brescia, R.; Povia, M.; Prato, M.; Bertoni, G.; Manna, L.; Moreels, I. Synthesis of Uniform Disk-Shaped Copper Telluride Nanocrystals and Cation Exchange to Cadmium Telluride Quantum Disks with Stable Red Emission. *J. Am. Chem. Soc.* **2013**, *135*, 12270–12278.
29. Beberwyck, B. J.; Surendranath, Y.; Alivisatos, A. P. Cation Exchange: A Versatile Tool for Nanomaterials Synthesis. *J. Phys. Chem. C* **2013**, *117*, 19759–19770.
30. Rivest, J. B.; Jain, P. K. Cation Exchange on the Nanoscale: An Emerging Technique for New Material Synthesis, Device Fabrication, and Chemical Sensing. *Chem. Soc. Rev.* **2013**, *42*, 89–96.
31. Son, D. H.; Hughes, S. M.; Yin, Y.; Alivisatos, A. P. Cation Exchange Reactions in Ionic Nanocrystals. *Science* **2004**, *306*, 1009–1012.
32. Jain, P. K.; Amirav, L.; Aloni, S.; Alivisatos, A. P. Nanoheterostructure Cation Exchange: Anionic Framework Conservation. *J. Am. Chem. Soc.* **2010**, *132*, 9997–9999.
33. Luther, J. M.; Zheng, H.; Sadtler, B.; Alivisatos, A. P. Synthesis of PbS Nanorods and Other Ionic Nanocrystals of Complex Morphology by Sequential Cation Exchange Reactions. *J. Am. Chem. Soc.* **2009**, *131*, 16851–16857.
34. Li, H.; Zanella, M.; Genovese, A.; Povia, M.; Falqui, A.; Giannini, C.; Manna, L. Sequential Cation Exchange in Nanocrystals: Preservation of Crystal Phase and Formation of Metastable Phases. *Nano Lett.* **2011**, *11*, 4964–4970.
35. van der Stam, W.; Gantapara, A. P.; Akkerman, Q. A.; Soligno, G.; Meeldijk, J. D.; van Roij, R.; Dijkstra, M.; de Mello Donega, C. Self-Assembly of Colloidal Hexagonal Bipyramid- and Bifrustum-Shaped ZnS Nanocrystals into Two-Dimensional Superstructures. *Nano Lett.* **2014**, *14*, 1032–1037.
36. Gupta, S.; Kershaw, S. V.; Rogach, A. L. 25th Anniversary Article: Ion Exchange in Colloidal Nanocrystals. *Adv. Mater.* **2013**, *25*, 6923–6944.
37. Moon, G. D.; Ko, S.; Min, Y.; Zeng, J.; Xia, Y.; Jeong, U. Chemical Transformations of Nanostructured Materials. *Nano Today* **2011**, *6*, 186–203.
38. Guo, W.; chen, N.; Tu, Y.; Dong, C.; Zhang, B.; Hu, C.; Chang, J. Synthesis of Zn-Cu-In-S/ZnS Core/Shell Quantum Dots with Inhibited Blue-Shift Photoluminescence and Applications for Tumor Targeted Bioimaging. *Theranostics* **2013**, *3*, 99–108.
39. Park, J.; Kim, S.-W. $CuInS_2$/ZnS Core/Shell Quantum Dots by Cation Exchange and Their Blue-Shifted Photoluminescence. *J. Mater. Chem.* **2011**, *21*, 3745–3750.
40. Beberwyck, B. J.; Alivisatos, A. P. Ion Exchange Synthesis of III-V Nanocrystals. *J. Am. Chem. Soc.* **2012**, *134*, 19977–19980.
41. Xie, Y.; Riedinger, A.; Prato, M.; Casu, A.; Genovese, A.; Guardia, P.; Sottini, S.; Sangregorio, C.; Miszta, K.; Ghosh, S.; *et al.* Copper Sulfide Nanocrystals with Tunable Composition by Reduction of Covellite Nanocrystals with $Cu^+$ Ions. *J. Am. Chem. Soc.* **2013**, *135*, 17630–17637.
42. Lesnyak, V.; George, C.; Genovese, A.; Prato, M.; Casu, A.; Ayyappan, S.; Scarpellini, A.; Manna, L. Alloyed Copper Chalcogenide Nanoplatelets *via* Partial Cation Exchange Reactions. *ACS Nano* **2014**, *8*, 8407–8418.
43. De Trizio, L.; Li, H.; Casu, A.; Genovese, A.; Sathya, A.; Messina, G. C.; Manna, L. Sn Cation Valency Dependence in Cation Exchange Reactions Involving $Cu_{2-x}Se$ Nanocrystals. *J. Am. Chem. Soc.* **2014**, *136*, 16277–16284.
44. Pan, D. C.; An, L. J.; Sun, Z. M.; Hou, W.; Yang, Y.; Yang, Z.; Lu, Y. F. Synthesis of Cu-In-S ternary nanocrystals with tunable structure and composition. *J. Am. Chem. Soc.* **2008**, *130*, 5620–5621.
45. Lide, D. R. *CRC Handbook of Chemistry and Physics*, 84th ed.; CRC Press: Boca Raton, 2003−2004.
46. Groeneveld, E.; Witteman, L.; Lefferts, M.; Ke, X.; Bals, S.; Van Tendeloo, G.; de Mello Donega, C. Tailoring ZnSe-CdSe Colloidal Quantum Dots *via* Cation Exchange: From Core/Shell to Alloy Nanocrystals. *ACS Nano* **2013**, *7*, 7913–7930.
47. Haram, S. K.; Quinn, B. M.; Bard, A. J. Electrochemistry of CdS Nanoparticles: A Correlation between Optical and Electrochemical Band Gaps. *J. Am. Chem. Soc.* **2001**, *123*, 8860–8861.
48. Ji, S.; Shi, T.; Qiu, X.; Zhang, J.; Xu, G.; Chen, C.; Jiang, Z.; Ye, C. A Route to Phase Controllable $Cu_2ZnSn(S_{1-x}Se_x)_4$ Nanocrystals with Tunable Energy Bands. *Sci. Rep.* **2013**, *3*, 2733.
49. Amelia, M.; Lincheneau, C.; Silvi, S.; Credi, A. Electrochemical Properties of CdSe and CdTe Quantum Dots. *Chem. Soc. Rev.* **2012**, *41*, 5728–5743.
50. Ahmadi, M.; Pramana, S. S.; Batabyal, S. K.; Boothroyd, C.; Mhaisalkar, S. G.; Lam, Y. M. Synthesis of $Cu_2SnSe_3$ Nanocrystals for Solution Processable Photovoltaic Cells. *Inorg. Chem.* **2013**, *52*, 1722–1728.
51. Zhong, H.; Lo, S. S.; Mirkovic, T.; Li, Y.; Ding, Y.; Li, Y.; Scholes, G. D. Noninjection Gram-Scale Synthesis of Monodisperse Pyramidal $CuInS_2$ Nanocrystals and Their Size-Dependent Properties. *ACS Nano* **2010**, *4*, 5253–5262.